Research Article Vol. 12, No. 9 / September 2025 / Optica 1357

Tailoring ultrahigh index plasmonic combinatorial metamaterials for SEIRA and SERS by tuning the fill fraction

Nicolas Spiesshofer,[1] Elle Wyatt,[1] Zoltan Sztranyovszky,[2] Caleb Todd,[1] Taras V. Mykytiuk,[1] James W. Beattie,[1] Rowena Davies,[1] Rakesh Arul,[1] Viv Lindo,[3] Thomas F. Krauss,[4] Angela Demetriadou,[2] and Jeremy J. Baumberg[1,*]

[1]NanoPhotonics Centre, Cavendish Laboratory, Department of Physics, JJ Thomson Avenue, University of Cambridge, Cambridge, CB3 0US, UK
[2]School of Physics and Astronomy, University of Birmingham, Birmingham B15 2TT, UK
[3]Analytical Sciences, BioPharmaceuticals Development, R&D, AstraZeneca, Cambridge, UK
[4]School of Physics, Engineering and Technology, University of York, York, YO10 5DD, UK
*jjb12@cam.ac.uk

Received 7 May 2025; revised 26 July 2025; accepted 28 July 2025; published 22 August 2025

Plasmonic materials with strong mid-infrared resonances allow enhanced molecular sensing, but obtaining the required high field enhancements in easily constructed geometries is challenging. Multilayer aggregates (MLaggs) of close-packed gold nanoparticles (AuNPs) exhibit strong extinction resonances that enhance both surface-enhanced Raman (SERS) and IR absorption (SEIRA) spectroscopies. Here, we show that these simply fabricated MLaggs behave as low-loss high refractive index (n) metamaterials in the mid-infrared and that they can reach a refractive index of $n > 10$. By admixing silver nanoparticles (AgNPs) with AuNPs and co-aggregating them, we demonstrate combinatorial metamaterials with near-perfect absorption and controlled linewidth. By selective dissolution, we are able to control the aggregate fill fraction and tune both the SEIRA resonance and the refractive index. Dissolution of the AgNPs leads to more porous aggregates, which enable adsorption and detection of larger analytes, making MLaggs useful for healthcare sensing applications.

https://doi.org/10.1364/OPTICA.567324

1. INTRODUCTION

Small molecule sensing with infrared absorption spectroscopy reveals molecular signatures that can be used for non-invasive optical characterization of a wide range of organic and inorganic compounds [1]. However, infrared (IR) spectroscopy has been constrained by poor detection sensitivity in aqueous media and especially in human matrices, making it hard to sense compounds at trace concentrations *in situ* compared to background interference [2].

Appropriately chosen metal nanostructures can locally enhance and confine mid-IR (MIR) light, hugely increasing light–matter interactions and giving rise to surface-enhanced IR absorption (SEIRA) spectroscopies. SEIRA can sense at lower concentrations than traditional IR spectroscopy techniques [3–5], due to the selective amplification of vibrational signatures of molecules located within enhancement hotspots of these nanostructures, depending on their coupling with plasmonic or dielectric resonances [6–8]. These resonances can be tuned in a variety of ways, including nanostructure shape [9–11], size [12,13], periodicity [14], material [15], and near-field coupling [16,17]. The SEIRA enhancement is thus closely linked to the architecture of the substrate. Since gold is inert and easily surface-functionalized, it has been frequently used in such plasmonic substrates [18]. A wide range of analytes readily adsorb onto these surfaces, including small biomolecules [19,20], pharmaceuticals [21], nano-, and microplastics [22]. Gold metal substrates have also been used to sense more complex biomolecules, such as membrane proteins and antibodies [23–26]. Traditionally, top-down fabrication methods such as electron-beam lithography have been used for gold MIR-resonant substrates, for instance, nanorods or nanodisk arrays, yielding large plasmonic SEIRA enhancements of up to 10^6 (for molecules in the enhanced field) with Q-factors of up to ~ 6 [27–34]. However, top-down lithographic methods are slow and costly for producing the ultrasmall gaps (~ 1 nm) that give high enhancements, so bottom-up methods are desirable.

Gold nanoparticles can be easily self-assembled into aggregates, which strongly enhance molecular vibrational resonances in the visible and mid-infrared. Their plasmonic resonances can be tuned depending on nanoparticle size, array geometry [35], and spacing [36], supporting both SERS and SEIRA [37]. In particular, self-assembled AuNP aggregates yield strong extinctions and SEIRA

enhancement [5,38,39], yet they have been difficult to characterize due to their broad parameter space [12], and analytical models typically have large numbers of fitting parameters. Chemically assembled aggregates are disordered, which affects their optical response in the visible and mid-infrared [40,41]. Fully ordered plasmonic superlattices with resonances in the infrared are highly desirable but difficult to fabricate due to particle polydispersity, which controls faceting, and control of gap sizes, leading to local disorder, which affects the MIR resonance [42–44]. Finally, incorporation of larger analytes in the optical hotspots can be inhibited due to their tortuosity and small gap size [45].

Here, we report how self-assembled AuNP multilayer aggregates (MLaggs) can be understood and utilized as robust high refractive index metamaterials [13,38]. Previous work has suggested the potential for self-assembled substrates incorporating nanoparticles with different morphologies to achieve high refractive indices [35,46,47] in the mid-infrared. Nanoparticle arrays with narrow and consistent gaps that support strong plasmonic enhancement [38,48] are here shown to act as an effective medium in the MIR, enabling rapid optimization of their optical properties [49]. For wavelengths $\lambda > 2\ \mu m$, the real part of the medium effective permittivity becomes essentially non-dispersive and can exceed $\mathrm{Re}(\varepsilon_{\mathrm{eff}}) > 10$, even reaching 100 with low loss. Our model predicts key features, including a strongly enhanced refractive index for small gaps <5 nm, potential for low-loss $\mathrm{Im}(n_{\mathrm{eff}}) < 0.1$, and a distinctive dependence on metal fill fraction and number of layers. This provides a tunable refractive index which sets the resonance wavelengths of a thin MLagg slab [35]. By constructing aggregates out of a mixture of Au and Ag nanoparticles, we develop an enhanced combinatorial metamaterial with a tunable refractive index. Subsequently dissolving these AgNPs out of the aggregate further tunes the fill factor and the aggregate resonance in a controlled manner, in good agreement with the metamaterial model. Finally, we find that these structures have direct applications, as their increased porosity together with a high index improves SEIRA sensing of >10 nm size analytes, such as biomolecules and colloids, in the mid-infrared fingerprint region.

2. RESULTS AND DISCUSSION

A. Modeling AuNP Aggregates as Metamaterials with an Effective Index

Previous work has shown the ability to tune the resonance of layered AuNP aggregates ("MLaggs"). Individual cycles of self-assembly can aggregate 1–2 close-packed layers of AuNPs on a liquid–liquid interface using the rigid cucurbit[5]uril (CB[5]) molecular spacer [50]. The CB[5] gives precise 0.9 nm gaps between all AuNPs (confirmed previously for single dimers [51]), leading to high field confinement and strong extinction [38]. Tight spacing of the nanoparticles leads to a strong enhancement of both IR and Raman molecular vibrational spectra [38,52], enabling surface-enhanced infrared and Raman spectroscopies (SEIRA and SERS). Stacking successive deposition cycles gives MLagg slabs with MIR resonances.

For a typical MLagg [Figs. 1(a)–1(c), AuNP diameter $D = 100$ nm, gap size $d = 0.9$ nm, and four deposition cycles], the SEIRA resonances of CB[5] in the nanogaps appear as asymmetric Fano resonances and vary in amplitude with detuning from the MLagg resonance [Fig. 1(b)]. By sequentially depositing layers of AuNPs, the plasmonic resonance of the aggregate is red-shifted

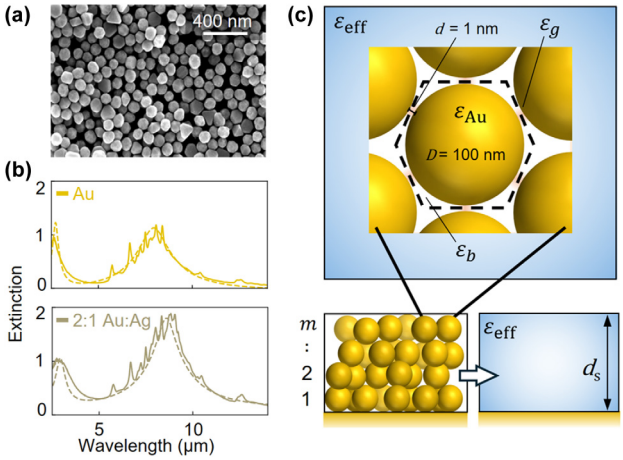

Fig. 1. (a) SEM of AuNP MLagg. (b) An extinction spectrum of pure AuNP MLagg and 2:1 Au:AgNP mixed MLagg [solid line, shown referenced to an Au mirror as $\log_{10}(R_{\mathrm{MLagg}}/R_{\mathrm{Au}})$] and a metamaterial model fit (dashed, see text). (c) A hexagonal lattice of AuNPs of 100 nm diameter and a gap size $d = 1$ nm forming AuNP MLagg with an effective medium $\varepsilon_{\mathrm{eff}}$ and a thickness L on a gold mirror.

into the molecular fingerprint region [38], and a close-packed layered AuNP structure is formed. This MLagg combines three material permittivities [Fig. 1(c)]: the AuNP ($\varepsilon_{\mathrm{Au}}$, large and negative in the IR), the organic linker molecules in the nanogaps ($\varepsilon_g \sim 2.3$), and the background permittivity (ε_b, typically water or air). We now discuss how these permittivities combine to make a metamaterial.

Previous treatments of MLagg layers modeled them as coupled plasmons with a near-linear dispersion relation [38] approximated by an effective refractive index n_{eff}, but with a number of arbitrary parameters. Now using full electromagnetic simulations of nanoparticles of diameter D in a hexagonal lattice with gap spacing d filled by the refractive index $n_g = \sqrt{\varepsilon_g}$ [Fig. 1(c)], we show that this effective index n_{eff} concept works well and attains extremely high values, thus showing MLaggs can form excellent low-loss metamaterials in the mid-infrared regime. The resonance now appears naturally as the Fabry–Pérot resonance of a slab of this metamaterial with thickness d_s (Fig. 1) and can be tuned in various ways.

From the reflection and transmission spectra (Fig. S1 in Supplement 1), we extract [53] the complex $n_{\mathrm{eff}}(\lambda)$ for a single close-packed nanoparticle layer (1ML) [Fig. 2(a)], and also show it for two stacked layers (2ML), where the upper layer is displaced laterally to retain close packing (Fig. S1 in Supplement 1). In the visible region, several resonances are seen due to a breakdown of the effective medium approximation as the wavelength λ approaches the nanoparticle diameter D. For $\lambda > 2\ \mu m$, however, where $\lambda \gg D$, the effective refractive index concept can be applied and shows that n_{eff} can attain large values while being almost dispersionless from $\lambda = 3-12\ \mu m$ [Fig. 2(a)]. Extracting the real and imaginary parts of n_{eff} as a function of gap size at $\lambda = 4\ \mu m$ [Fig. 2(b)] shows that for smaller gaps, when the NP fill fraction f increases, n_{eff} grows rapidly, exceeding $n_{\mathrm{eff}} > 4$ for typical nanogaps in our samples.

Previous models for dense mixtures of metal with dielectric have been challenging to obtain, with the Bruggeman effective medium model [54] only valid for $f < 0.3$ for the MLagg architecture. The Maxwell–Garnet effective medium model, which is expected to

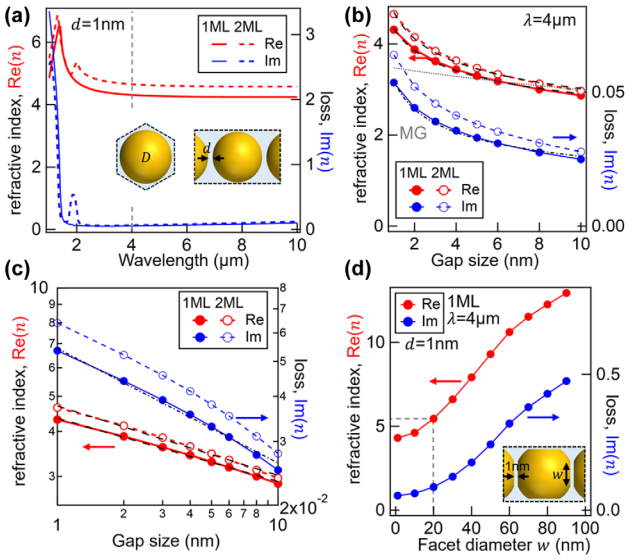

Fig. 2. (a) Extracted real and imaginary parts of the effective refractive index of hexagonal-close-packed AuNPs, diameter $D = 100$ nm, spaced by $d = 1$ nm, for one (solid) or two (dashed) nanoparticle layers. (b) and (c) Extracted n_{eff} at $\lambda = 4$ μm, for varying gap size d. Gray dotted line is the Maxwell–Garnett model of Re(n_{eff}) for 1ML. Dashed lines are fits from Eq. (3). (d) Scaling of n_{eff} at $\lambda = 4$ μm and $d = 1$ nm for increasing facets width w (shown in inset). A dashed line shows typical experimental facet size.

work reasonably for large fill fractions provided that randomly arranged spherical particles radiate as dipoles [55] ($D \ll \lambda$) takes the form

$$\varepsilon_{\text{MG}} = \varepsilon_g \frac{3\varepsilon_g + (1+2f)(\varepsilon_{\text{Au}} - \varepsilon_g)}{3\varepsilon_g + (1-f)(\varepsilon_{\text{Au}} - \varepsilon_g)}. \tag{1}$$

Since in the mid-infrared, $|\varepsilon_{\text{Au}}| \gg \varepsilon_g$, this reduces to

$$\varepsilon_{\text{MG}} = \varepsilon_g \frac{1+2f}{1-f}. \tag{2}$$

While for larger gaps of $d > 5$ nm, the Maxwell–Garnett description accounts reasonably for the effective refractive index [Fig. 2(b), gray dotted line], it underestimates n_{eff} for smaller gaps, since the dipole-like behavior of each NP breaks down [13]. The increasing concentration of the optical field in smaller nanogaps now dominates the combined response, further enhancing the polarizability and hence the net refractive index. For small NP gaps ($d \ll D$), we find the phenomenological scaling [Fig. 2(c)]

$$n_{\text{eff}}/n_g = 3.9\left[\sqrt{f}d^{-q} + i0.017 f d^{-2q}\right], \tag{3}$$

with power exponent $q = 0.17$, independent of fill fraction f [solid lines in Figs. 2(b) and 2(c)]. In a simple model based on confinement of light in nanogaps [56], the gap field should scale as $1/d$, thus suggesting that $q = 0.5$, which is much larger than that found here from full simulations. We find that the effective refractive index increases strongly as the interparticle gap size decreases, which is in agreement with previous findings for the optical regime [46,47,49,57]. For stacked MLagg layers, the fill fraction increases toward 74% for touching NPs, giving effective refractive indices exceeding 5, much larger than almost any dielectric material (including silicon), and with a loss contribution of less than <0.05. These values can lead to metal architectures capable of $Q > 100$, which is extremely unusual.

The metamaterial refractive index is further enhanced when the gaps between the NPs are faceted, as is the case for almost all nanoparticles, since even spherical nanoparticles are resculpted by a variety of external forces within plasmonic systems, including strong van der Waals attraction and optical fields, interactions with linker molecules, or photochemically [58–61]. Extracting n_{eff} as the facets grow drastically enhances the refractive index, which can now exceed $n_{\text{eff}} > 10$ for accessible geometries without inducing excessive loss [Fig. 2(d)], which is in agreement with literature for visible-range optically resonant metallic metamaterials [46]. This low loss arises from the ultrasmall gaps, which provide extreme light confinement with high in-plane k that reduces optical penetration into the metal facets [56].

A slab of this effective metamaterial (multilayer of MLagg) acts as a simple Fabry–Pérot cavity, with high interface reflectivity R arising from the large n_{eff}. Resonances at $\lambda_p = 2n_{\text{eff}}L/p$ (for $p = 1, 2, \ldots$) are thus observed [Fig. 1(b)]. By experimentally measuring these MLaggs with a profilometer (Fig. S2 in Supplement 1), we identify the MLagg thickness L, which matches that expected for these multilayers. Hence, we can extract the resulting effective medium n_{eff} and loss, noting a slight increase in the refractive index of these metamaterials for higher layer thickness. The Fabry–Pérot modes probed in this effective metamaterial have been previously described and depend on the effective refractive index as well as layer thickness. The strongest SEIRA enhancement, which is localized to the gaps between nanoparticles, has enhancement factors of up to 10^6 [12,38]. Simultaneously, these structures also exhibit a single-nanogap plasmonic resonance in the near-infrared, supporting SERS enhancement of $\sim 10^6$ [39,52].

For the lowest-order resonance, the quality factor Q in a Fabry–Pérot cavity is a function of its reflectivity, which is related to the effective refractive index for its fundamental resonance (Section S4 in Supplement 1 for derivation):

$$Q \simeq \frac{\pi\sqrt{R}}{1-R} = \frac{\pi}{4}\left(n_{\text{eff}} - \frac{1}{n_{\text{eff}}}\right) \simeq \frac{\pi}{4} n_{\text{eff}}. \tag{4}$$

Measured Q values from different samples currently range from 2 to 3 and provide an independent way to quantify the effective refractive index. These values are currently limited by missing NPs in the films [Fig. 1(a)], which decreases f and hence n_{eff} as well as increasing the loss through disorder-induced scattering. Experiments are underway to optimize this; however, we also note that higher Q is not necessarily helpful for SEIRA since it reduces the available bandwidth.

Modeling the MLaggs as effective media allows their study for different compositions and organizations. While the current low-cost high-throughput MLagg production yields gap size, fill fraction, and disorder as above, further tuning is available by incorporating different nanoparticles, as now discussed.

B. Gold and Silver Co-Aggregation and Dissolution to Control Fill Fraction

In addition to gold, silver nanoparticles (AgNPs) are widely used in plasmonics, partly for their photocatalytic properties as well as in diagnostics and therapeutics. Indeed, alloys of Au and Ag in different ratios allow some grading of the optical and catalytic properties

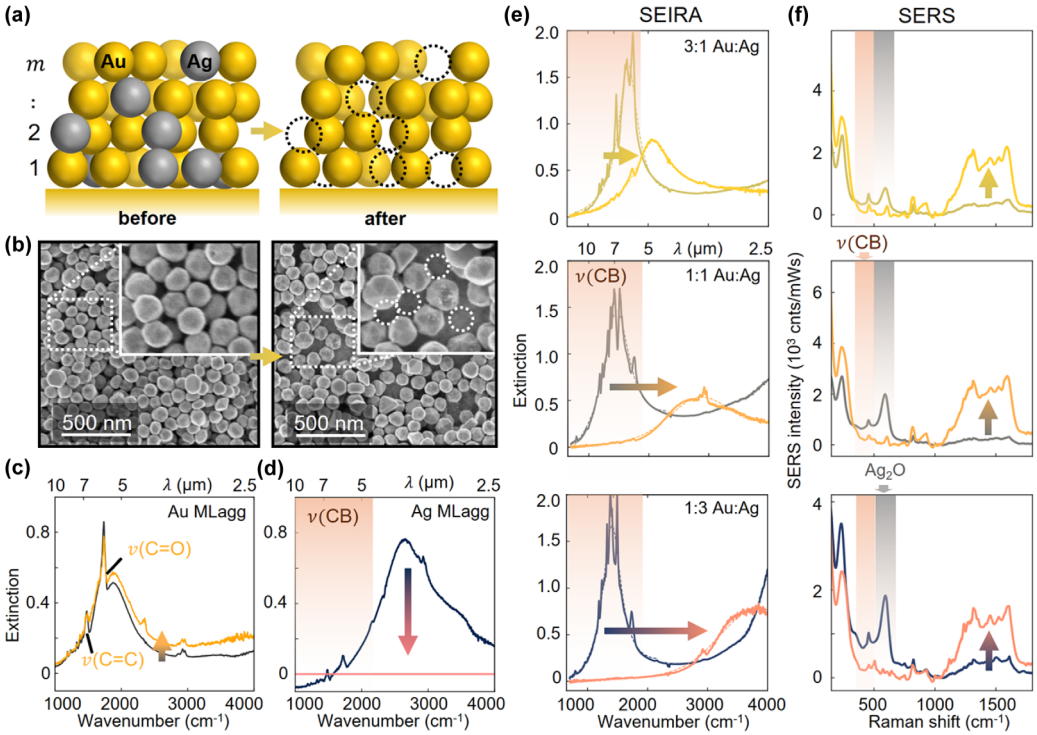

Fig. 3. (a) Au–Ag mixed MLagg before and after dissolution of AgNPs, leaving voids (dotted) in porous Au MLagg. (b) SEMs before and after AgNP dissolution. (c)–(e) SEIRA spectra of (c) AuNP control, (d) AgNP MLagg, and (e) for different Au:Ag mix ratios, before (gray) and after (color) dissolution. Arrows indicate the main changes. (f) SERS spectra from MLaggs of different Au:Ag ratios before and after dissolution. All NP MLaggs are $D = 100$ nm and $d = 0.9$ nm.

[62]. Here, we instead use the combination of pure AuNPs and AgNPs to create mixed MLaggs, by co-aggregating them (Fig. 3).

Citrate-capped AgNPs can be aggregated by the same method as AuNPs (Fig. S3a in Supplement 1), and their MLaggs have resonances with a similar Q-factor and extinction to AuNP aggregates [Fig. 3(d)]. SEM images (Fig. S3 in Supplement 1) show a similar structural morphology to the AuNP aggregates. The characteristic peaks of the aggregating molecule CB[5] appear in both the SEIRA and SERS spectra (Fig. 3), indicating that aggregates with AgNPs successfully self-assemble. We note that while the localized surface plasmonic resonance of silver occurs at a shorter wavelength than that of gold, MLagg resonances shift into the infrared, where there is little difference in their optical permittivity.

By first mixing gold and silver metal nanoparticles in solution, then co-aggregating with CB[5] at the liquid–liquid interface and depositing MLagg multilayers, a "combinatorial metamaterial" (mixed Au/Ag MLagg) is formed. This material has a similar structure to the pure-gold aggregates ["before," Figs. 3(a) and 3(b)] and combines the plasmonic properties of both noble metals. SEM images evidence a similar assembly to MLaggs of one metal alone. An increasingly purple aggregate color is seen in bright-field (BF) imaging as the ratio of AgNPs increases (Fig. S4 in Supplement 1); however, the resonances in SEIRA remain similar [Fig. 3(e)]. AgNPs are then etched out from the MLaggs by immersion in 30% NH_4OH, further confirmed by SEM and energy-dispersive X-ray ["after," Figs. 3(a) and 3(b); Figs. S5 and S6 in Supplement 1]. The NH_4OH etches away surface-bound silver oxide (Ag_2O) by forming silver–ammonia coordination complexes without sintering the MLagg nanogaps. The resulting structures have increased porosity and lower fill fraction.

C. SEIRA and SERS Track Plasmonic Resonances and Fill Fraction-Dependent Tuning

The effects of dissolution on the optical properties of the aggregate are studied using SEIRA, SERS, and dark-field spectroscopy. SEIRA spectra show that the resonances of Au–Ag MLaggs blueshift when the AgNPs are dissolved. The shift increases with the amount of Ag in the initial aggregate [Fig. 3(e); Fig. S7 in Supplement 1]. When the pure Ag sample is immersed in NH_4OH, the SEIRA spectrum vanishes as the AgNPs are fully dissolved out [Fig. 3(d)]. Since no shift is observed for similarly treated pure gold MLaggs [Fig. 3(c)], we conclude that these shifts occur solely from silver dissolution. The infrared resonance can thus be simply tuned by changing the Au–Ag ratio and thus the number of voids formed in the aggregate.

The initial Au–Ag ratio also controls the post-dissolution porosity, while the SEIRA and SERS show that the AuNPs remain structurally intact and the plasmonic gaps are maintained [Figs. 3(e) and 3(f)]. After dissolution [Figs. 3(c)–3(f); Fig. S7 in Supplement 1], the vibrational signal from CB[5] decreases by $\sim 50\%$ for all Au–Ag ratios (including the pure gold control sample). New absorption peaks emerge in the molecular fingerprint region, as well as SERS peaks $\sim$1500 cm^{-1}, corresponding to dissolution products of the reaction. The decrease in the CB[5] SEIRA signal is also due to the gradual detuning of the plasmonic resonance.

Dark-field (DF) spectroscopy gives additional information about the short-range aggregate structure. The DF peak position of the mixed MLagg is blue-shifted by $\sim 7\%$ relative to the pure gold control (Fig. S7 in Supplement 1) due to the reduced plasmon coupling along such heterogeneous chains [63]. This alters the field

enhancements, modifying SERS intensities. After dissolution, the DF peak position red-shifts, assuming roughly the same value as for the pure gold control sample. This suggests that AgNPs no longer "short out" the longer AuNP chains. The SERS spectra for Au–Ag samples before dissolution show strong Ag_2O peaks [64,65] at ~ 600 cm^{-1} (Fig. 3(f) gray shaded, absent in gold control), which are stronger for higher AgNP fractions (Fig. S8 in Supplement 1) [66]. After silver dissolution, the Ag_2O peak disappears, as expected from etching the surface-bound Ag_2O.

Electrochemical regeneration of the post-dissolution aggregate reverses the effects of NH_4OH and reinserts CB[5] molecules into the plasmonic hotspots (Section 4) [52]. By oxidizing and reducing the nanogap in 1 M phosphate buffer and 1 mM CB[5], ammonia and silver degradation products are removed from the nanogaps, and CB[5] molecules are replaced. In SERS, the CB[5] signals from the 2:1 porous MLagg sample are fully restored (Fig. S9). Plasma oxidation gives similar effects, removing silver dissolution products from the nanogap without sintering it (Fig. S10 in Supplement 1) [39]. The MLagg can then be rescaffolded with many different molecules, which replace the gold oxide now plugging the nanogaps [39].

D. Resonance Properties of Au–Ag Mixed Aggregates

We study these SEIRA resonance shifts across a wide range of Au–Ag ratios to precisely tune the fill fraction of the resulting porous Au MLaggs (Fig. 4). For increasing AgNP concentrations, the resonance peak shifts further to the blue on dissolution (full spectra in Fig.S7 in Supplement 1). While an initial mix of $s = 3{:}1$ Au:Ag gives resonance spectral shifts $\sim 30\%$, this increases more than fivefold to $\sim 150\%$ for $s = 1{:}3$ Au:Ag. These % shifts are independent of the initial resonance position [Fig. 4(b)], which is set by the nanoparticle diameter and number of multilayers, indicating structural stability. The fill fraction of the AuNP aggregate is thus a reliable predictor of the MLagg resonance position.

The model of Eq. (2) can account for these shifts through the decreasing fill fraction in the metamaterial. An approximate analytical expression based on the Maxwell–Garnett approximation (Section S4 in Supplement 1 for derivation) for the expected shift in resonance position $\Delta\lambda_p$ from the initial Ag:Au ratio s is

$$\left(1+\frac{\Delta\lambda_p}{\lambda_p}\right)^2 \simeq \frac{1-\frac{s}{1-1/f}}{1-\frac{s}{1+1/2f}}. \tag{5}$$

While this fits the data reasonably for an initial fill factor of $f = 0.7$ [Fig. 4(a), line], it slightly underestimates the changes in resonance position at higher concentrations. This is likely due to partial collapse of the aggregate thickness after etching for high AgNP concentrations, as seen in SEMs (Fig. S11 in Supplement 1). In these samples, we find that the model of Eq. (2) yields an effective medium refractive index $n_{\text{eff}} \approx 3.0$ for the $s = 2:1$ combinatorial metamaterial [as fit in Fig. 1(a)], using measured layer thicknesses (Fig. S2 in Supplement 1).

The peak MIR extinction of mixed aggregates with AgNPs almost doubles compared to the Au controls [Fig. 4(d)], reaching near-complete extinction ($R_{\min} \sim 1\%$) and leading to a two-fold increase in the strength of the CB[5] molecular vibrational resonances. Our metamaterial slab model indicates this arises when the destructively interfering reflections from the top and bottom MLagg surfaces become equal in amplitude. This suggests that absorption or scattering increases when including AgNPs (since otherwise the lower reflection is stronger than the upper reflection). Indeed, the shape, size, and facet inhomogeneity of AgNPs is considerably more than for the AuNPs, which can cause this effect (Fig. S3a in Supplement 1). After etching the AgNPs, the extinction of the porous Au MLagg drops $\sim 50\%$ to the same value as of the control AuNP MLagg, showing that facet inhomogeneities are an important design parameter and strongly affect MLagg loss. The dark-field spectra further suggest changes in structure as AgNPs are dissolved out. The DF resonance linewidths increase for Ag ratios $>25\%$ as a more porous structure is created, though less effect is seen for the highest mixture ratios (Fig. S12 in Supplement 1).

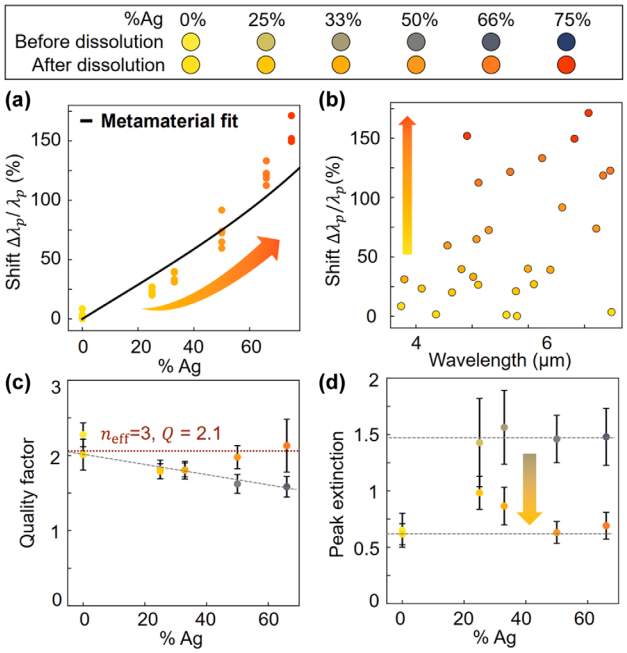

Fig. 4. (a) Fractional shift (%) in resonance peak position versus initial AgNP concentration s, together with an analytical metamaterial (MM) model (line), and (b) versus initial wavelength. (c) and (d) Changes from Ag dissolution versus initial AgNP concentration s for (c) the Q-factor (data points overlap for 25% and 33%) with a computed refractive index from the MM model and the Q-factor (red dotted), and (d) peak extinction (dashed lines are a guide to the eye).

In our slab model of the MLagg metamaterial, the Q of the resonance relates to the refractive index through Eq. (4). Indeed, as this suggests, an increase in the refractive index leads to an increase in the sharpness of the MIR resonance. Hence, by contrast, when higher concentrations of silver nanoparticles are etched out of the Au/Ag MLagg, the larger decrease in fill fraction leads to more broadening of the resonance compared to the pure gold control [Fig. 4(c)]. For $n_{\text{eff}} \approx 3$, as extracted for $s = 2:1$, this predicts a Q-factor of $\sim$2.1, which reasonably matches the data [Fig. 4(c)] but is lower than the expected quality factor from the metamaterials model (Fig. 2). We presume that structural disorder in the combinatorial metamaterial currently affects the resonance linewidth, which is evidenced by a decrease in the Q-factor as the concentration of AgNPs increases. Moreover, the large spot size of the IR beam (50×50 μm^2) relative to the NP size spectrally averages over the structural roughness of the MLagg (rms roughness $R_a \approx 74$ nm for 9 monolayers of ~ 725 nm height, Fig. S2 in Supplement 1), which further broadens the spectrum.

We note that tuning can also be obtained by stacking alternating single layers of Au and Ag MLaggs (Fig. S13 in Supplement 1).

When dissolving the Ag MLaggs out, the Au MLagg layers collapse on top of each other, retaining the original porosity but decreasing the metamaterial slab thickness, and thus tuning the MIR resonance to higher wavenumbers as expected.

E. Enhanced Sensing from Porous MLaggs

In addition to providing a method to tune the dispersion of MLaggs, adding voids to the aggregate creates a more porous structure. This many-fold increased porosity enhances the diffusion coefficient of analytes into the aggregate. For larger molecules with low diffusivity, a reduced MLagg tortuosity facilitates diffusion into aggregate hotspots [45,68] and subsequent adsorption to the Au surfaces.

To demonstrate this, we detect 2.5 mgml^{-1} 50 nm diameter amine(NH)-functionalized polystyrene (PS) nanoparticles, which are too large to bind within void-less MLagg structures. We use PS NPs here as a well-characterized proxy analyte that cannot change shape (unlike proteins, which can denature). The PS nanoparticles attach to the AuNP surface via N-hydroxysuccinimide (NHS) and carbodiimide (EDC) covalent cross-linking [69]. To prepare aggregates for functionalization, we rescaffold $s = 2:1$ porous Au MLagg and $s = 0$ Au control MLagg using 3-mercaptoproprionic acid (MPA) after cleaning by plasma oxidation (Section 4). This completely removes both CB[5] and side products, while characteristic peaks of MPA appear in the SEIRA and SERS spectra, including the $\sim 1415\ \mathrm{cm}^{-1}$ $\upsilon(\mathrm{C-O-H})$ and $\sim 1735\ \mathrm{cm}^{-1}$ $\upsilon(\mathrm{C=O})$ vibrations from the exposed carboxylic acid [70] [Figs. 5(c) and 5(d)]. Subsequent functionalization of the Au surfaces with NHS and EDC leads to the emergence of the new $\upsilon(\mathrm{COO-NHS})$ peak at $1745\ \mathrm{cm}^{-1}$ due to binding of the NHS ester group to the exposed carboxylic acid. The emergence of this peak serves as a key indicator for the successful binding of NHS to the AuNP surface-bound carboxyl groups of MPA (Fig. S14 in Supplement 1).

Subsequent immersion of these functionalized MLaggs in a buffered solution (pH 7.5) of NH-capped PS nanoparticles reveals additional peaks due to the formation of a stable amide bond. Characteristic $\delta(\mathrm{C-H})$ polystyrene peaks [71] emerge at $\sim 700\ \mathrm{cm}^{-1}$, while the peak amplitude of the $\sim 1400\ \mathrm{cm}^{-1}$ vibrations doubles compared to the control sample [Figs. 5(c) and 5(d); Fig. S15 in Supplement 1]. This $\upsilon(\mathrm{C-H})$ peak is characteristic of C–H groups immediately adjacent to the amine functional group. Additional polystyrene $\upsilon(\mathrm{C=C})$ peaks at 1450 and $1490\ \mathrm{cm}^{-1}$ are stronger in the porous MLagg. At the same time, the $1745\ \mathrm{cm}^{-1}$ line decreases, indicating loss of NHS ester groups (COO-NHS) as the PS binds. Further indication of stronger binding is given by the SERS spectrum of the porous MLaggs [Figs. 5(e) and 5(f)]. The peak at $\sim 1000\ \mathrm{cm}^{-1}$, which appears after the addition of PS, is the polystyrene ring-bending mode [67]. The magnitude of this signal is nearly threefold stronger in the porous than in the control sample. We also find stronger PS SERS signals for porous MLaggs with different fill fractions ($s = 3:1$ and $s = 1:1$; Fig. S16 in Supplement 1). These data indicate a stronger uptake of polystyrene nanoparticles when voids are present and show that the porous nanostructure is also well-suited to analyze compounds that are significantly larger than the nm-sized gap between nanoparticles. Further, we note that the enhancement from these structures is critical to sense PS nanoparticles at such low concentrations, as evidenced by the minimal PS signal when they are deposited instead on clean flat gold (Fig. S17 in Supplement 1).

We find that the polystyrene beads do not bind close enough to MLagg plasmonic hotspots in aggregates without functionalization of the Au surfaces (Fig. S18 in Supplement 1). Moreover, alternative functionalization of the AuNPs with 4-nitro-thiophenol (4-NTP) does not lead to the emergence of the characteristic peaks of polystyrene, as this molecular monolayer repels amine-capped PS nanoparticles (Fig. S19 in Supplement 1).

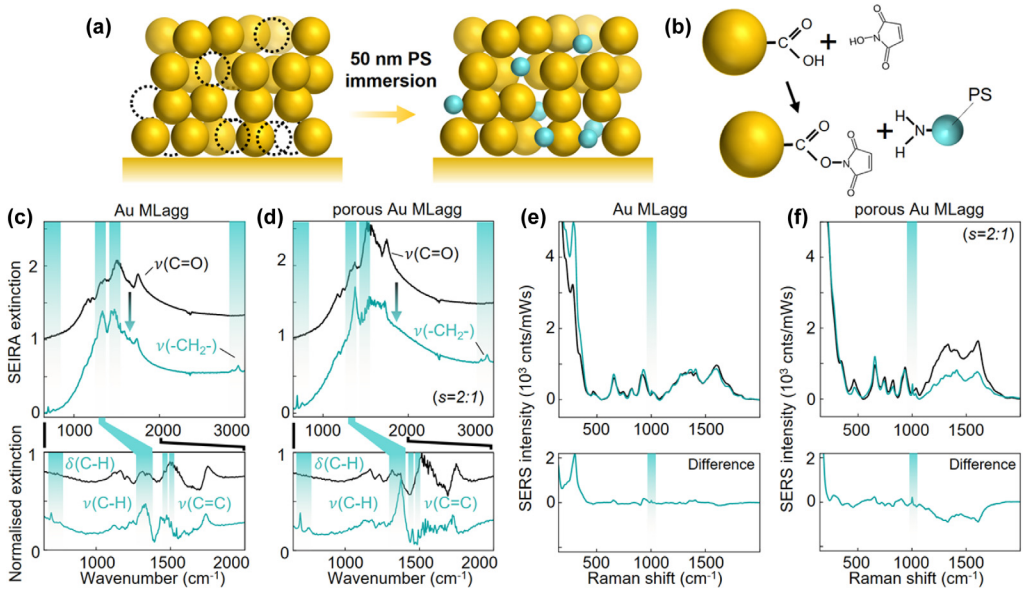

Fig. 5. (a) Binding of amine-capped polystyrene (PS) nanoparticles (blue) within voids (dotted circles) after dissolving AgNPs. (b) NHS binding to carboxyl-modified surface of AuNPs, with subsequent binding to amine-capped PS. (c) and (d) SEIRA spectra after plasma oxidation and addition of MPA + EDC-NHS (black), and after further addition of PS nanoparticles (blue), for (c) control Au MLagg sample (no silver) and (d) porous Au MLagg ($s = 2:1$). Lower graphs show SEIRA after background removal. e,f) SERS spectra before (black) and after (cyan) addition of PS nanoparticles for (e) the gold MLagg control sample and (f) porous Au MLagg ($s = 2:1$), with the $1000\ \mathrm{cm}^{-1}$ PS ring-breathing mode [67] indicated in cyan. Lower graphs show difference between the two traces.

The functionalization of the MLagg Au surfaces with EDC-NHS significantly aids in binding PS to the surface. Suitable surface coatings are thus able to selectively bring different classes of analytes down onto these MLagg sensing surfaces.

3. CONCLUSION

We demonstrate here that bottom-up assembled AuNP multilayer aggregates can be designed to be excellent MIR metamaterials. Consistent ultra-narrow gaps between the constituent nanoparticles as well as larger facets lead to simulated refractive indices exceeding 10, with Q-factors >20. These metamaterial slab structures exhibit resonances in the mid-infrared, which are desirable for biological, chemical, and environmental sensing [72,73]. Since the refractive index of the MLaggs is set by the nanoscale architecture, this governs the resonance linewidth as well as its spectral position.

Experimentally, co-aggregating Au and Ag NPs yields combinatorial metamaterials with high refractive index, which give Fabry–Pérot MIR resonances of controlled linewidth and high extinction (reflectivities $\leq 1\%$), highlighting the strong effect of faceting on the MLagg loss. We find that the Q-factor of these structures yields a reasonable estimate of their refractive index. The molecular vibrations of all molecules (such as the CB[5] gap linker) experience stronger light–matter interactions on resonance, thus significantly enhancing SEIRA and SERS signals. By using combinatorial metamaterials of NPs, these MLaggs can be re-tuned by dissolving out AgNPs from a predefined NP mix ratio in the MLagg, thus controlling their fill factor, which in turn predictably tunes the resonance peaks of the slab. Moreover, using chemical and electrochemical rescaffolding allows for the introduction of other linker molecules for sensing [39,52]. Metamaterial simulations show significant promise for future augmentation of the effective refractive index. Facet homogeneity, ultrasmall gap sizes, tighter packing, and increased NP size are all shown to increase the MLagg refractive index.

Finally, incorporating AgNPs, which are subsequently dissolved out, gives structures with higher porosity and lower tortuosity, making them useful for sensing >10 nm-sized analytes, such as nanoplastics. Higher porosities shift the resonance peaks away from the molecular fingerprint region, limiting how porous the structure can be for practical sensing applications. This trade-off between refractive index and tortuosity of these MLaggs can likely be influenced by the NP size and geometry, now under further investigation. We also find EDC-NHS chemistry within the gaps can be directly tracked using SEIRA, thus opening up a wide range of sensing modalities with optimized capabilities.

4. MATERIALS AND METHODS

A. Tunable Multilayer Aggregate Formation

Gold nanoparticles (100 nm, BBI Solutions) and silver (100 nm, Sigma Aldrich) nanoparticles are mixed in an Eppendorf tube with a sonicator for 1 min to make up a total of 500 μL of nanoparticle solution by combining in ratios from $s = 1{:}0$, 3:1, 2:1, 1:1, 2:1, 1:3, and 0:1. A total of 500 μL of chloroform ($CHCl_3$) is then added to another Eppendorf, followed by 500 uL of the nanoparticle mixture. A total of 100 μL of 1 mM cucurbit[5]uril (CB[5]) solution is then added and shaken for ~ 1 min to initiate aggregation. The mixture is left to settle so that the immiscible $CHCl_3$ and aqueous phases separate, and the aggregated AuNPs move to the interfaces (chloroform–aqueous and aqueous–air). The aqueous phase is washed with three 300 μL aliquots of DI water to dilute the citrate salts and other supernatants and then concentrated by careful removal of the aqueous phase to form a ~ 5 μL aggregate droplet floating on the $CHCl_3$. The droplet is deposited onto a pre-cleaned gold-coated silicon substrate (100 nm Au and 5 nm Cr on silicon) and left to dry. Once dried, the resulting AuNP/AgNP multilayer aggregate (MLagg) is rinsed with DI water and dried with N_2. This is repeated another three times, depositing each aggregate droplet in the same spatial position each time for a total of four depositions to give a sample with multiple layers of nanoparticles (MLagg).

B. Dissolution

To dissolve the AgNPs, samples are immersed in 30% NH_4OH solution overnight, then rinsed with DI water and dried with N_2.

C. Plasma Cleaning

The MLaggs are oxygen plasma cleaned for 45 min (oxygen mass flow of 30 sccm, 90% RF power) using a plasma etcher (Diener electronic GmbH & Co. KG) to remove CB[5], citrate, and other supernatants from the AuNP surfaces (verified using SERS). To re-introduce a scaffolding ligand, the MLaggs are either immersed in equal volumes of 1 mM CB[5] or CB[7] solution and 1 M HCl for 5 min, or in 10 mM BPT in ethanol for 30 min. In both cases, the MLaggs are rinsed with DI water and dried with N_2.

D. Functionalization

The control and porous AuNP aggregates are inserted into a plasma etcher for 30 min to remove bound species and replace the AuNP surface with gold oxide. Subsequently, the aggregates are immersed in 10 mM mercapto-proprionic acid diluted in ethanol for 30 min. The aggregates are washed with DI water and immersed in a solution of 50 mM NHS, 50 mM EDC, 1 M NaCl, pH 6.0, for 30 min. The aggregates are washed with DI water and immersed in 2.5 $mgml^{-1}$ 50 nm polystyrene in 100 mM KPB, pH 7.0 for 20 h. Finally, the samples are rinsed with isopropanol and water and immersed in 1 M ethanolamine for 5 min to quench unreacted ester functional groups, with subsequent rinsing.

E. Electrochemical Regeneration

The MLaggs are deposited on fluorine-doped tin oxide (FTO). Then they are immersed in an electrochemical flow cell. This cell is fabricated from 10:1 PDMS:cross-linker, and its geometry is adjusted to include a well, inlet, and outlet, as well as inserts for electrodes. The three-electrode amperometric system includes a Pt counter electrode and an Ag/AgCl reference electrode. The samples are used as the working electrode, contacted with Cu tape, and immersed in the flow cell with 1 M potassium phosphate buffer at pH 7.5. A constant potential of 1.5 V is applied for 60 s, followed by a rinsing step. Subsequently, the samples are immersed in 1 M potassium phosphate buffer and 1 mM CB[5], and a potential of −0.8 V is applied for 15 s. Finally, the samples are rinsed with DI water.

F. Infrared Microscopy

All samples are measured in a Shimadzu AIM-9000 infrared microscope, linked to a Shimadzu IR-Tracer 100. For image acquisition, a spectral resolution of 4 cm^{-1}, an aperture size of 50 × 50 μm^2, and an averaging number of 200 are used. Spectra of the aggregates are registered to the same spot in the bright field for dissolution, cleaning, and functionalization. Post-processing involves filtering with a Savitzky–Golay filter. Background plasmonic resonances are fitted using a Voigt fit with constrained peak resonance, and the resonance position, maximum extinction, and Q-factor are extracted.

G. Raman Microscopy

SERS measurements are collected on a Renishaw InViva Raman confocal microscope, using a 20× objective (NA = 0.4) and 1200 lines mm^{-1} grating. To collect the lower wavenumber spectral regions, the 785 nm excitation laser is used in extended scan mode, with 1 s integration time and a laser power of 2.2 mW at the sample. All measurements are taken at room temperature, and the spectra are spectrally calibrated with respect to Si. Spectra are analyzed using a Python code, and any background is removed by iteratively fitting a polynomial to the base of the peaks.

H. Dark-Field Microscopy

Dark-field (DF) scattering spectra are taken in reflection on a custom set-up consisting of an Olympus BX51 and an Ocean Optics QE-Pro spectrometer. All spectra are collected with a 20× Olympus objective with 500 ms integration time. DF spectra of MLagg samples are collected across a 10 × 10 point grid with 50 μm spacing to cover a total sample area of 500 × 500 μm^2. All spectra are referenced to a white light scattering target (Labsphere).

I. Characterization

Scanning electron microscope (SEM) imaging of MLaggs deposited on gold substrates uses an FEI Philips Dualbeam Quanta 3D SEM (dwell 3–10 μs, HV 2 kV, current 50 pA, and ≈ 2.0 mm WD). Additionally, SEM images and EDX maps were acquired with an FEI Nova NanoSEM (dwell 3–10 μs, HV 10 kV, ≈ 4.0 mm WD.

J. Simulations

To calculate the effective refractive index of the homogenized material, we use COMSOL Multiphysics (v6.0). The simulation domain is a hexagonal unit cell, with Floquet periodic boundary conditions applied on the sides and a perfectly matched layer applied at the top and bottom. An incoming port is added at the bottom to launch the excitation and obtain the complex reflection coefficient, and an outgoing port is added at the top to obtain the complex transmission coefficient. The ports are set to be half a wavelength away from the metamaterial layer. The metamaterial layer is set in air, and it consists of the plasmonic gold resonator with diameter D, embedded in a slab of refractive index $n = 1.5$, thickness d_s. The permittivity of gold is given by a Drude–Lorenz model with set parameters as in [74], which provides a good fit for gold permittivity [75] in the observed wavelength ranges.

Funding. Engineering and Physical Sciences Research Council (EP/L015978/1, EP/X037770/1, EP/Y008162/1, EP/L015889/1, EP/S022953/1, EP/Y008774/1, EP/X012689/1, EP/Y036379/1, EP/S02297X/1); H2020 European Research Council (883703); AstraZeneca; Gates Cambridge Trust (OPP1144); Royal Society (URF/R1/180097, URF/R/231024, RGF/EA/181038).

Acknowledgment. The authors acknowledge financial support from the European Research Council (ERC) under Horizon 2020 research and innovation programme PICOFORCE (Grant Agreement No. 883703) and from the EPSRC (Cambridge NanoDTC EP/L015978/1, EP/X037770/1, EP/Y036379/1, EP/Y008162/1). N.S. acknowledges support from EPSRC Grant EP/L015889/1 for the EPSRC Centre for Doctoral Training in Sensor Technologies and Applications, and from AstraZeneca (MedImmune Ltd). C.T. is supported by a Gates Cambridge fellowship (OPP1144). R.A. acknowledges support from the Winton Programme for the Physics of Sustainability and from St. John's College Cambridge. R.D. acknowledges support from EPSRC grant EP/S022953/1 for the EPSRC Centre for Doctoral Training in Integrated Functional Nano. A.D. and Z.S. wish to acknowledge support from the Royal Society University Research Fellowship URF/R1/180097 and URF/R/231024, the Royal Society Research Fellows Enhancement Award RGF/EA/181038, and funding from ESPRC Grants EP/Y008774/1 and EP/X012689/1 from EPSRC for the CDT in Topological Design EP/S02297X/1. Contributions: N.S., E.W., and J.J.B. conceived and designed the experiments. N.S. and E.W. performed the fabrication and spectroscopic experiments with input from T.V.M., with R.D. and C.T. aiding the characterization. N.S. and E.W. analyzed the data with input from J.J.B., R.A., T.F.K., and J.W.B. Z.S. and C.T. carried out simulations and the analytical modeling. All authors contributed to writing and editing the manuscript.

Disclosures. The authors J.J.B., R.A., and E.W. declare the following competing interests: filed patent, surface-enhanced spectroscopy substrates, UK 2304765.7, 30/3/2023. The authors N.S., Z.S., C.T., T.V.M., J.W.B., R.D., V.L., T.F.K., and A.D. declare no competing interests.

Data availability. The data that support the findings of this study are available from the Cambridge Open Data archive [76] and from the corresponding author upon reasonable request.

Supplemental document. See Supplement 1 for supporting content.

REFERENCES

1. P. Griffiths and J. Haseth, *Fourier Transform Infrared Spectrometry*, 2nd ed. (2006).
2. D. Li, C. Xu, J. Xie, *et al.*, "Research progress in surface-enhanced infrared absorption spectroscopy: from performance optimization, sensing applications, to system integration," Nanomaterials (Basel) **13**, 2377 (2023).
3. M. Osawa, "Surface-enhanced infrared absorption," in *Near-Field Optics and Surface Plasmon Polaritons*, S. Kawata, ed. (Springer, 2001), pp. 163–187.
4. H.-L. Wang, E.-M. You, R. Panneerselvam, *et al.*, "Advances of surface-enhanced Raman and IR spectroscopies: from nano/microstructures to macro-optical design," Light Sci. Appl. **10**, 161 (2021).
5. J. Kundu, F. Le, P. Nordlander, *et al.*, "Surface enhanced infrared absorption (SEIRA) spectroscopy on nanoshell aggregate substrates," Chem. Phys. Lett. **452**, 115–119 (2008).
6. F. Neubrech, A. Pucci, T. W. Cornelius, *et al.*, "Resonant plasmonic and vibrational coupling in a tailored nanoantenna for infrared detection," Phys. Rev. Lett. **101**, 157403 (2008).
7. A. John-Herpin, A. Tittl, L. Kühner, *et al.*, "Metasurface-enhanced infrared spectroscopy: an abundance of materials and functionalities," Adv. Mater. **35**, 2110163 (2023).
8. S. Kharratian, D. Conteduca, B. Procacci, *et al.*, "Metasurface-enhanced mid-infrared spectroscopy in the liquid phase," Chem. Sci. **13**, 12858–12864 (2022).
9. T. R. Jensen, R. P. Van Duyne, S. A. Johnson, *et al.*, "Surface-enhanced infrared spectroscopy: a comparison of metal island films with discrete and nondiscrete surface plasmons," Appl. Spectrosc. **54**, 371–377 (2000).
10. K. Chen, R. Adato, and H. Altug, "Dual-band perfect absorber for multispectral plasmon-enhanced infrared spectroscopy," ACS Nano **6**, 7998–8006 (2012).

11. J. Wei, Y. Li, Y. Chang, *et al.*, "Ultrasensitive transmissive infrared spectroscopy via loss engineering of metallic nanoantennas for compact devices," ACS Appl. Mater. Interfaces **11**, 47270–47278 (2019).
12. N. S. Mueller, E. Pfitzner, Y. Okamura, *et al.*, "Surface-enhanced Raman scattering and surface-enhanced infrared absorption by plasmon polaritons in three-dimensional nanoparticle supercrystals," ACS Nano **15**, 5523–5533 (2021).
13. S. J. Palmer, X. Xiao, N. Pazos-Perez, *et al.*, "Extraordinarily transparent compact metallic metamaterials," Nat. Commun. **10**, 2118 (2019).
14. K. Weber, M. L. Nesterov, T. Weiss, *et al.*, "Wavelength scaling in antenna-enhanced infrared spectroscopy: toward the far-IR and THz region," ACS Photonics **4**, 45–51 (2017).
15. W. J. Chang, B. J. Roman, A. M. Green, *et al.*, "Surface-enhanced infrared absorption spectroscopy by resonant vibrational coupling with plasmonic metal oxide nanocrystals," ACS Nano **18**, 20636–20647 (2024).
16. C. Huck, F. Neubrech, J. Vogt, *et al.*, "Surface-enhanced infrared spectroscopy using nanometer-sized gaps," ACS Nano **8**, 4908–4914 (2014).
17. J. Chae, B. Lahiri, and A. Centrone, "Engineering near-field SEIRA enhancements in plasmonic resonators," ACS Photonics **3**, 87–95 (2016).
18. J. Zheng, X. Cheng, H. Zhang, *et al.*, "Gold nanorods: the most versatile plasmonic nanoparticles," Chem. Rev. **121**, 13342–13453 (2021).
19. W.-J. Bao, J. Li, J. Li, *et al.*, "Au/ZnSe-based surface enhanced infrared absorption spectroscopy as a universal platform for bioanalysis," Anal. Chem. **90**, 3842–3848 (2018).
20. R. Semenyshyn, F. Mörz, T. Steinle, *et al.*, "Pushing down the limit: in vitro detection of a polypeptide monolayer on a single infrared resonant nanoantenna," ACS Photonics **6**, 2636–2642 (2019).
21. S. B. Yaqoob, R. Adnan, R. M. Rameez Khan, *et al.*, "Gold, silver, and palladium nanoparticles: a chemical tool for biomedical applications," Front. Chem. **8**, 376 (2020).
22. G. Xu, H. Cheng, R. Jones, *et al.*, "Surface-enhanced Raman spectroscopy facilitates the detection of microplastics <1 μm in the environment," Environ. Sci. Technol. **54**, 15594–15603 (2020).
23. K. Ataka, S. T. Stripp, and J. Heberle, "Surface-enhanced infrared absorption spectroscopy (SEIRAS) to probe monolayers of membrane proteins," Biochim. Biophys. Acta BBA Biomembr. **1828**, 2283–2293 (2013).
24. D. Kavungal, P. Magalhães, S. T. Kumar, *et al.*, "Artificial intelligence–coupled plasmonic infrared sensor for detection of structural protein biomarkers in neurodegenerative diseases," Sci. Adv. **9**, eadg9644 (2023).
25. E. Pfitzner, H. Seki, R. Schlesinger, *et al.*, "Disc antenna enhanced infrared spectroscopy: from self-assembled monolayers to membrane proteins," ACS Sens. **3**, 984–991 (2018).
26. R. Adato, A. A. Yanik, J. J. Amsden, *et al.*, "Ultra-sensitive vibrational spectroscopy of protein monolayers with plasmonic nanoantenna arrays," Proc. Natl. Acad. Sci. **106**, 19227–19232 (2009).
27. I. M. Pryce, Y. A. Kelaita, K. Aydin, *et al.*, "Compliant metamaterials for resonantly enhanced infrared absorption spectroscopy and refractive index sensing," ACS Nano **5**, 8167–8174 (2011).
28. F. Neubrech, C. Huck, K. Weber, *et al.*, "Surface-enhanced infrared spectroscopy using resonant nanoantennas," Chem. Rev. **117**, 5110–5145 (2017).
29. T. G. Mayerhöfer and J. Popp, "Periodic array-based substrates for surface-enhanced infrared spectroscopy," Nanophotonics **7**, 39–79 (2018).
30. C. D'Andrea, J. Bochterle, A. Toma, *et al.*, "Optical nanoantennas for multiband surface-enhanced infrared and Raman spectroscopy," ACS Nano **7**, 3522–3531 (2013).
31. L. V. Brown, K. Zhao, N. King, *et al.*, "Surface-enhanced infrared absorption using individual cross antennas tailored to chemical moieties," J. Am. Chem. Soc. **135**, 3688–3695 (2013).
32. J. Chae, B. Lahiri, J. Kohoutek, *et al.*, "Metal-dielectric-metal resonators with deep subwavelength dielectric layers increase the near-field SEIRA enhancement," Opt. Express **23**, 25912 (2015).
33. Z. Ren, Z. Zhang, J. Wei, *et al.*, "Wavelength-multiplexed hook nanoantennas for machine learning enabled mid-infrared spectroscopy," Nat. Commun. **13**, 3859 (2022).
34. L. Paggi, A. Fabas, H. El Ouazzani, *et al.*, "Over-coupled resonator for broadband surface enhanced infrared absorption (SEIRA)," Nat. Commun. **14**, 4814 (2023).
35. R. Kim, K. Chung, J. Y. Kim, *et al.*, "Metal nanoparticle array as a tunable refractive index material over broad visible and infrared wavelengths," ACS Photonics **5**, 1188–1195 (2018).
36. F. Le, D. W. Brandl, Y. A. Urzhumov, *et al.*, "Metallic nanoparticle arrays: a common substrate for both surface-enhanced Raman scattering and surface-enhanced infrared absorption," ACS Nano **2**, 707–718 (2008).
37. M. Baia, F. Toderas, L. Baia, *et al.*, "Multilayer structures of self-assembled gold nanoparticles as a unique SERS and SEIRA substrate," ChemPhysChem **10**, 1106–1111 (2009).
38. R. Arul, D.-B. Grys, R. Chikkaraddy, *et al.*, "Giant mid-IR resonant coupling to molecular vibrations in sub-nm gaps of plasmonic multilayer metafilms," Light Sci. Appl. **11**, 281 (2022).
39. D.-B. Grys, M. Niihori, R. Arul, *et al.*, "Controlling atomic-scale restructuring and cleaning of gold nanogap multilayers for surface-enhanced Raman scattering sensing," ACS Sens. **8**, 2879–2888 (2023).
40. Z. M. Sherman, J. Kang, D. J. Milliron, *et al.*, "Illuminating disorder: optical properties of complex plasmonic assemblies," J. Phys. Chem. Lett. **15**, 6424–6434 (2024).
41. A. M. Green, W. J. Chang, Z. M. Sherman, *et al.*, "Structural order and plasmonic response of nanoparticle monolayers," ACS Photonics **11**, 1280–1292 (2024).
42. H. Wang, J. Kundu, and N. J. Halas, "Plasmonic nanoshell arrays combine surface-enhanced vibrational spectroscopies on a single substrate," Angew. Chem. Int. Ed. **46**, 9040–9044 (2007).
43. F. Schulz, O. Pavelka, F. Lehmkühler, *et al.*, "Structural order in plasmonic superlattices," Nat. Commun. **11**, 3821 (2020).
44. L. Dong, X. Yang, C. Zhang, *et al.*, "Nanogapped Au antennas for ultrasensitive surface-enhanced infrared absorption spectroscopy," Nano Lett. **17**, 5768–5774 (2017).
45. M. J. Skaug, L. Wang, Y. Ding, *et al.*, "Hindered nanoparticle diffusion and void accessibility in a three-dimensional porous medium," ACS Nano **9**, 2148–2156 (2015).
46. J.-H. Huh, J. Lee, and S. Lee, "Soft plasmonic assemblies exhibiting unnaturally high refractive index," Nano Lett. **20**, 4768–4774 (2020).
47. N. Kim, J. Huh, Y. Cho, *et al.*, "Achieving optical refractive index of 10-plus by colloidal self-assembly," Small **20**, 2404223 (2024).
48. J.-M. Nam, J.-W. Oh, H. Lee, *et al.*, "Plasmonic nanogap-enhanced Raman scattering with nanoparticles," Acc. Chem. Res. **49**, 2746–2755 (2016).
49. D. Doyle, N. Charipar, C. Argyropoulos, *et al.*, "Tunable subnanometer gap plasmonic metasurfaces," ACS Photonics **5**, 1012–1018 (2018).
50. R. W. Taylor, T.-C. Lee, O. A. Scherman, *et al.*, "Precise subnanometer plasmonic junctions for SERS within gold nanoparticle assemblies using Cucurbit[n]uril "Glue,"," ACS Nano **5**, 3878–3887 (2011).
51. B. De Nijs, R. W. Bowman, L. O. Herrmann, *et al.*, "Unfolding the contents of sub-nm plasmonic gaps using normalising plasmon resonance spectroscopy," Faraday Discuss. **178**, 185–193 (2015).
52. S. M. Sibug-Torres, D.-B. Grys, G. Kang, *et al.*, "In situ electrochemical regeneration of nanogap hotspots for continuously reusable ultrathin SERS sensors," Nat. Commun. **15**, 2022 (2024).
53. X. Chen, T. M. Grzegorczyk, B.-I. Wu, *et al.*, "Robust method to retrieve the constitutive effective parameters of metamaterials," Phys. Rev. E **70**, 016608 (2004).
54. J. A. Dolan, M. Saba, R. Dehmel, *et al.*, "Gyroid optical metamaterials: calculating the effective permittivity of multidomain samples," ACS Photonics **3**, 1888–1896 (2016).
55. P. Mallet, C. A. Guérin, and A. Sentenac, "Maxwell-Garnett mixing rule in the presence of multiple scattering: derivation and accuracy," Phys. Rev. B **72**, 014205 (2005).
56. J. J. Baumberg, J. Aizpurua, M. H. Mikkelsen, *et al.*, "Extreme nanophotonics from ultrathin metallic gaps," Nat. Mater. **18**, 668–678 (2019).
57. K. Chung, R. Kim, T. Chang, *et al.*, "Optical effective media with independent control of permittivity and permeability based on conductive particles," Appl. Phys. Lett. **109**, 021114 (2016).
58. F. Yin, R. Palmer, and Q. Guo, "Nanoscale surface recrystallization driven by localized electric field," Phys. Rev. B **73**, 073405 (2006).
59. B. Song, J. Jansen, F. D. Tichelaar, *et al.*, "In-situ transmission electron microscopy and first-principles study of Au (100) surface dislocation dynamics," Surf. Sci. **608**, 154–164 (2013).
60. C. Guo, P. Benzie, S. Hu, *et al.*, "Extensive photochemical restructuring of molecule-metal surfaces under room light," Nat. Commun. **15**, 1928 (2024).

61. A. Xomalis, R. Chikkaraddy, E. Oksenberg, *et al.*, "Controlling optically driven atomic migration using crystal-facet control in plasmonic nanocavities," ACS Nano **14**, 10562–10568 (2020).
62. S. Link, Z. L. Wang, and M. A. El-Sayed, "Alloy formation of gold−silver nanoparticles and the dependence of the plasmon absorption on their composition," J. Phys. Chem. B **103**, 3529–3533 (1999).
63. C. Tserkezis, R. W. Taylor, J. Beitner, *et al.*, "Optical response of metallic nanoparticle heteroaggregates with subnanometric gaps," Part. Part. Syst. Charact. **31**, 152–160 (2014).
64. Y. Yin, Z.-Y. Li, Z. Zhong, *et al.*, "Synthesis and characterization of stable aqueous dispersions of silver nanoparticles through the Tollens process," Electronic supplementary information (ESI) available: photographs of silver mirror, and of stable dispersions of silver nanoparticles from mixing diluted silvering solutions under sonication at various times," See http://www.rsc.org/suppdata/jm/b1/b107469e/, J. Mater. Chem. **12**, 522–527 (2002).
65. G. I. N. Waterhouse, G. A. Bowmaker, and J. B. Metson, "The thermal decomposition of silver (I, III) oxide: a combined XRD, FT-IR and Raman spectroscopic study," Phys. Chem. Chem. Phys. **3**, 3838–3845 (2001).
66. X. Lu and E. Masson, "Formation and stabilization of silver nanoparticles with Cucurbit[n]urils (n = 5–8) and cucurbituril-based pseudorotaxanes in aqueous medium," Langmuir **27**, 3051–3058 (2011).
67. X.-X. Zhou, R. Liu, L.-T. Hao, *et al.*, "Identification of polystyrene nanoplastics using surface enhanced Raman spectroscopy," Talanta **221**, 121552 (2021).
68. R. Raccis, A. Nikoubashman, M. Retsch, *et al.*, "Confined diffusion in periodic porous nanostructures," ACS Nano **5**, 4607–4616 (2011).
69. K. K. Zeming, N. V. Thakor, Y. Zhang, *et al.*, "Real-time modulated nanoparticle separation with an ultra-large dynamic range," Lab. Chip **16**, 75–85 (2016).
70. S. Sam, L. Touahir, J. Salvador Andresa, *et al.*, "Semiquantitative study of the EDC/NHS activation of acid terminal groups at modified porous silicon surfaces," Langmuir **26**, 809–814 (2010).
71. A. S. Patole, S. P. Patole, J. Yoo, *et al.*, "Effective *in situ* synthesis and characteristics of polystyrene nanoparticle-covered multiwall carbon nanotube composite," J. Polym. Sci. Part B Polym. Phys. **47**, 1523–1529 (2009).
72. A. J. El-Helou, Y. Liu, C. Chen, *et al.*, "Optical metasurfaces for the next-generation biosensing and bioimaging," Laser Photonics Rev. **19**, 2401715 (2025).
73. M. L. Brongersma, R. A. Pala, H. Altug, *et al.*, "The second optical metasurface revolution: moving from science to technology," Nat. Rev. Electr. Eng. **2**, 125–143 (2025).
74. E. Elliott, K. Bedingfield, J. Huang, *et al.*, "Fingerprinting the hidden facets of plasmonic nanocavities," ACS Photonics **9**, 2643–2651 (2022).
75. R. L. Olmon, B. Slovick, T. W. Johnson, *et al.*, "Optical dielectric function of gold," Phys. Rev. B **86**, 235147 (2012).
76. N. Spiesshofer, E. Wyatt, Z. Sztranyovszky, *et al.*, "Research data supporting "Tailoring ultrahigh index plasmonic combinatorial metamaterials for SEIRA and SERS by tuning the fill fraction" [Dataset]," Apollo - University of Cambridge Repository, 2025, https://doi.org/10.17863/CAM.120356.